Potential nighttime contamination of CERES Clear-Sky Field of View by Optically Thin Cirrus during the CRYSTAL-FACE campaign

Yong-Keun Lee[1], Ping Yang[1], Yongxiang Hu[2], Bryan A. Baum[2],
Norman G. Loeb[2,3], and Bo-Cai Gao[4]

1. Department of Atmospheric Sciences, Texas A&M University, College Station, Texas 77843
2. NASA Langley Research Center, Hampton, Virginia 23681
3. Hampton University, Hampton, Virginia
4. Remote Sensing Division, Naval Research Laboratory, Washington, DC

Revised manuscript (**MS ID#: JGR_2005JD006372**)
for publication in *J. Geophys. Res.*

Abstract

We investigate the outgoing broadband longwave (LW, 5~200 μm) and window (WIN, 8~12 μm) channel radiances at the top of atmosphere (TOA) under clear-sky conditions, using data acquired by the Cloud and the Earth's Radiant Energy System (CERES) and Moderate-Resolution Imaging Spectroradiometer (MODIS) instruments onboard the NASA Terra satellite platform. In this study, detailed analyses are performed on the CERES Single Scanner Footprint TOA/Surface Fluxes and Clouds product to understand the radiative effect of thin cirrus. The data are acquired over the Florida area during the Cirrus Regional Study of Tropical Anvils and Cirrus Layers – Florida Area Cirrus Experiment (CRYSTAL-FACE) field program. Of particular interest is the anisotropy associated with the radiation field. Measured CERES broadband radiances are compared to those obtained from rigorous radiative transfer simulations. Analysis of results from this comparison indicates that the simulated radiances tend to be larger than their measured counterparts, with differences ranging from 2.1% to 8.3% for the LW band and from 1.7% to 10.6% for the WIN band. The averaged difference in radiance is approximately 4% for both the LW and WIN channels. A potential cause for the differences could be the presence of thin cirrus (*i.e.*, optically thin ice clouds with visible optical thicknesses smaller than approximately 0.3). The detection and quantitative analysis of these thin cirrus clouds are challenging even with sophisticated multispectral instruments. While large differences in radiance between the CERES observations and the theoretical calculations are found, the corresponding difference in the anisotropic factors is very small (0.2%). Furthermore, sensitivity studies show that the influence due to a ±1 K bias of the surface temperature on the errors of the LW and WIN channel radiances is of the same order as that associated with a ±2% bias of the surface emissivity. The LW and WIN errors associated with a ±5% bias of water vapor amount in the lower atmosphere in conjunction with a ±50% bias of water vapor amount in the upper atmosphere is similar to that of a ±1 K bias of the vertical temperature profile. Even with the uncertainties considered for these various factors, the simulated LW and WIN radiances are still larger than the observed radiances if thin cirrus clouds are excluded.

1. Introduction

Thin cirrus clouds are widespread and radiatively important [e.g., *Chepfer et al*., 1998, 2001; *Gao et al*., 2002; *Mather et al*., 1998; *McFarquhar et al*., 2000; *Prabhakara et al*., 1993; *Rossow and Schiffer*, 1991; *Wang et al*., 1994, 1996; *Winker and Trepte*, 1998]. Several studies [*Dessler and Yang*, 2003; *Meyer et al*., 2004; *Roskovensky and Liou*, 2003; *Kahn et al*., 2005] show that optically thin cirrus properties can be inferred on the basis of satellite observations (e. g., the radiometric measurements acquired by MODIS or AIRS). In particular, *Dessler and Yang* [2003] further analyzed MODIS cloud-cleared data [*Ackerman et al*. 1998] over the oceans between 30°S and 30°N using the 1.375 μm channel. While the cirrus clouds were too tenuous for the data to be flagged as being cloudy using the operational cloud clearing procedure, the Tropical Western Pacific (TWP) region was shown to be an area where cirrus occurred with a high frequency, with optical thicknesses generally between 0.1 and 0.15. A substantial portion of the MODIS clear-sky pixels near Hawaii were contaminated by subvisual cirrus clouds. Note that subvisual cirrus clouds are defined to have optical thickness less than 0.03 by *Sassen et al*. [1989]. In terms of optical thickness, the operational lower threshold for cirrus detection based on the MODIS multispectral data is approximately 0.2-0.3 [*Dessler and Yang*, 2003]. The inability to adequately detect and analyze these thin cirrus clouds may lead to biases in the simulated longwave and window radiances in comparison with measurements.

The Clouds and the Earth's Radiant Energy System (CERES) [*Wielicki et al*., 1996] is one of the state-of-the-art scientific satellite instruments developed for NASA's Earth Observing System (EOS). Included in the CERES Single Scanner Footprint (SSF) products [*Geier et al*., 2003] are various parameters including the broadband radiances and the fluxes at the top-of-atmosphere (TOA) and the surface. Each CERES field of view (FOV) in the SSF product contains imager-based information on clear-sky conditions and/or cloud properties for up to two cloud layers, including cloud top height, cloud thermodynamic phase, cloud effective particle size, and cloud optical thickness.

The CERES instrument measures broadband filtered radiances in three channels: a total channel (0.3-200 μm), a shortwave channel (0.3-5 μm), and a window channel

(WIN, 8-12 μm) [*Lee et al.*, 1996]. The daytime longwave (LW, 5~200 μm) radiance is determined from the total, window, and shortwave channel measurements, whereas the nighttime LW radiance is derived from the total and window channel measurements [*Loeb et al.*, 2001]. The measured filtered radiances are converted to the corresponding unfiltered radiances before subsequent conversion to fluxes. The development of the CERES operational products also involves the Moderate Resolution Imaging Spectroradiometer (MODIS) cloud data for determining cloud properties within each CERES FOV [*Minnis et al.*, 1997; *Smith et al.*, 2004]. With the scene identification (including the surface features) provided in the CERES FOV, broadband radiances are converted to fluxes by using a set of angular distribution models (ADMs) [*Loeb et al.*, 2003b; *Loeb et al.*, 2005]. The LW broadband radiance decreases with increasing the viewing zenith angle. This feature is called the limb-darkening effect [*Loeb et al.*, 2003b; *Smith et al.*, 1994]. The conversion of unfiltered radiance to flux is based on an ADM that takes the limb darkening effect into account. For the CERES Terra SSF Edition-1A data, the ADMs developed for TRMM have been used [*Loeb et al.*, 2003b].

The advantage of the CERES SSF product is that it provides quantitative cloud information (e.g., the optical thickness). Given a vertical atmospheric profile that includes the vertical distributions of the atmospheric temperature and water vapor through the rawinsonde measurements, the CERES SSF product in conjunction with a rigorous radiative transfer model can be used for computing the column radiance and flux.

Motivated by the fact that the inability to adequately detect and analyze these thin cirrus clouds may lead to biases in the simulated LW and WIN radiances, this study investigates the potential contamination of CERES clear-sky FOVs by optically thin cirrus clouds. Additionally, the anisotropy factors associated with the CERES LW and WIN channel radiation fields are also investigated. The data involved in the present study were acquired during the Cirrus Regional Study of Tropical Anvils and Cirrus Layers-Florida Area Cirrus Experiment (CRYSTAL-FACE) campaign [*Jensen et al.*, 2004] in July 2002. Rawinsonde data obtained during the CRYSTAL-FACE campaign provide the necessary atmospheric profiles of temperature and humidity which are necessary for the

radiative transfer simulations for a direct comparison with the corresponding overpass CERES data.

With the scene identification information, including the surface emissivity [*Wilber et al.*, 1999] and surface skin temperature (SSF-59) for a CERES FOV, and the corresponding rawinsonde observation, the vertical structure of the absorption due to various radiatively important gases can be computed with the use of the HITRAN-2000 database [*Rothman et al.*, 1998]. Furthermore, with the gaseous absorption optical thickness, the discrete ordinate radiative transfer (DISORT) model [*Stamnes et al.*, 1988] can be used to compute the LW and WIN channel broadband radiances. The surface skin temperature is defined as MOA (Meteorological, Ozone, and Aerosols) surface temperature at a level of 2 cm below the surface over land and the surface skin temperature corresponds to the Reynold's Sea Surface Temperature (SST) [*Geier et al.*, 2003] over ocean.

The rest of this paper is organized as follows. Section 2 describes the data and methodology. Section 3 discusses the observed and calculated radiances, the optical thickness of thin cirrus clouds inferred from the differences between the two radiances, and the variation of the anisotropy factor values. The results of various sensitivity studies are shown in Section 4. Finally, conclusive remarks are provided in Section 5.

2. Data and Methodology

The rawinsonde data used in this study were acquired during the CRYSTAL-FACE campaign in July 2002 at four locations: Key West (24.5 N, 81.8 W), Miami (25.8 N, 80.4 W), Tampa (27.7 N, 82.4 W) (NWS stations) and Everglades City (25.844 N, 81.386 W) (Pacific Northwest Laboratory PARSL facility). For the radiative transfer simulations, the atmosphere sampled by each rawinsonde is divided into 100 layers. When the cloud fraction for a CERES FOV is less than 0.1%, the FOV is regarded as clear [*Loeb et al.*, 2003b]. CERES products provide clear percent coverage that indicates the coverage of clear condition within a FOV. In this study we consider only FOVs with a clear-sky coverage of at least 99.9%. In total, 76 FOVs are selected from different days

in July 2002 for a detailed study within an area of 0.25° x 0.25° in terms of the latitudes and longitudes around the four locations where the rawinsonde data were taken. The surface type is ocean for 33 FOVs and land for the other 43 FOVs. Of these, 74 FOVs are observed at night and 2 FOVs in daytime over ocean. The average height of the tropopause is 15.6 km and the mean temperature 199.2 K. The CERES SSF data (e.g., radiance, flux, emissivity, surface skin temperature) from the EOS Terra platform were used in this study.

The CERES cloud mask classification technique employs threshold tests that involve the radiances acquired at 0.64, 1.6, 3.7, 11, and 12 μm MODIS imager channels [*Minnis et al.*, 2003; *Trepte et al.*, 1999]. A MODIS pixel is declared as cloudy when at least one of these five channel radiances is significantly different from the corresponding expected clear sky radiance. MODIS pixels deemed as clear are categorized as weak and strong, or they can be classified as being filled with fire, smoke, or aerosol, or being affected by sunglint, or covered with snow. While all five channels can be used during the daytime, only three infrared channels, 3.7, 11, and 12 μm, are used at nighttime. The MODIS imager pixel results are convolved into each CERES FOV and subsequently are used to provide the cloud fraction within the CERES FOV.

In the present forward radiative transfer simulations, an optically thin cirrus layer is placed below the tropopause for a given clear-sky CERES FOV. The average geometrical cloud thickness is 0.5 km. An optically thin cirrus cloud located near the tropopause at extremely cold temperatures is assumed to consist solely of droxtals [*Yang et al.*, 2003a; *Zhang et al.*, 2004] for the theoretical light scattering and radiative transfer computations. Baum et al. [2005] discuss the use of *in situ* cirrus microphysical data from midlatitude synoptic cirrus and tropical anvil cirrus to develop bulk ice cloud scattering models. However, for ice clouds of extremely low optical thickness that are located just below the tropopause, the assumption is made that the particle size distributions are extremely narrow and centered at very small particle sizes. The single-scattering properties of droxtals are provided at 39 wavenumbers selected within a spectral region spanning from 50 to 2000 cm^{-1}, which are further interpolated for a high spectral resolution on the basis of a spline-interpolation technique. The extinction efficiency, absorption efficiency, and asymmetry factor are computed from the composite method developed by *Fu et al.*

[1999]. The technical details for the present light scattering computation are not described here, as they are similar to those reported by *Yang et al.* [2005].

To consider the effect of size distribution, we use the gamma distribution [*Hansen and Travis*, 1974], given as follows:

$$n(r) = \frac{N_0 (r_{eff} V_{eff})^{(V_{eff}-1)/V_{eff}}}{\Gamma[(1-2V_{eff})/V_{eff}]} r^{(1-3V_{eff})/V_{eff}} \times \exp(-r/r_{eff} V_{eff}), \quad (1)$$

where N_0 is the total number of the particles in unit volume. In Eq. (1), r_{eff} and V_{eff} are effective radius and variance (or, dispersion), respectively, which are given by

$$r_{eff} = \frac{\int_{r_1}^{r_2} r^3 n(r)\, dr}{\int_{r_1}^{r_2} r^2 n(r)\, dr}, \quad (2)$$

$$V_{eff} = \frac{\int_{r_1}^{r_2} (r - r_{eff})^2 r^2 n(r)\, dr}{r_{eff}^{\ 2} \int_{r_1}^{r_2} r^2 n(r) dr}. \quad (3)$$

The effective variance (V_{eff}) for various water clouds lies between 0.111 and 0.193 [*Hansen*, 1971]. In this study, a variance value of V_{eff} = 0.2 is used for cirrus. It is reasonable to choose an effective variance larger for an ice cloud than for a water cloud, as ice crystals in cirrus clouds tend to have broader size distributions than the distributions of water droplets in water clouds [*Mitchell*, 2002]. For a given size distribution, the mean values of the extinction efficiency, absorption efficiency, asymmetry factor, and effective diameter (D_e) are defined as follows:

$$< Q_e > = \frac{\int_{L_{\min}}^{L_{\max}} Q_e(L) A(L) n(L) dL}{\int_{L_{\min}}^{L_{\max}} A(L) n(L) dL}, \quad (4)$$

$$< Q_a >= \frac{\int_{L_{\min}}^{L_{\max}} Q_a(L)A(L)n(L)dL}{\int_{L_{\min}}^{L_{\max}} A(L)n(L)dL}, \quad (5)$$

$$< g >= \frac{\int_{L_{\min}}^{L_{\max}} g(L)Q_s(L)A(L)n(L)dL}{\int_{L_{\min}}^{L_{\max}} Q_s(L)A(L)n(L)dL}, \quad (6)$$

$$D_e = \frac{3}{2}\frac{\int_{L_{\min}}^{L_{\max}} V(L)n(L)dL}{\int_{L_{\min}}^{L_{\max}} A(L)n(L)dL}. \quad (7)$$

where *V(L)* is the volume and *A(L)* is the projected area of the particle with size of *L* (μm). Note that the definition of the effective particle size in Eq. (7) follows the work of *Foot* [1988], *Francis et al*. [1994], and *Fu* [1996], and is a generalization of the definition of the effective radius introduced by *Hansen and Travis* [1974] for water droplets. Furthermore, the definition of the effective particle size adopted in this study is consistent with that used in the operational MODIS cloud retrieval [*King et al*., 2003; *Platnick et al*., 2003].

Figure 1 shows the variation of the mean single-scattering properties for four particle sizes (D_e = 10, 20, 40 and 60 μm) as functions of the wavenumber of the incident radiation. Generally, the scattering properties of small particles are different from those of large particles because the scattering of radiation by small particles is closer to those for the regime of Rayleigh scattering [*Yang et al*., 2003b]. Additionally, the variation of the averaged absorption efficiency for smaller particle sizes is similar to that of the imaginary part of ice refractive index [see *Warren*, 1984].

A line-by-line (LBL) radiative transfer model developed by *Heidinger* [1998] is used for calculating the background optical depths of clear-sky atmospheric layers due to the absorption by various radiatively important gases (e.g. H_2O, CO_2, O_3, N_2O, CO, CH_4, etc.) with the line parameters from HITRAN-2000 [*Rothman et al*., 1998]. The continuum absorption of water vapor and other gases are considered on the basis of the approach developed by *Tobin et al*. [1999]. The broadband outgoing TOA LW and WIN

band radiances are calculated for each FOV using the DISORT [*Stamnes et al.*, 1988] implemented with 32 streams.

Following tradition in the liteature, we specify the optical thickness of a cirrus cloud in reference to its value at a visible wavelength, that is, the cirrus optical thickness in the LW spectrum can be specified as follows:

$$\tau = \frac{< Q_e >}{2} \tau_{vis} \tag{8}$$

where τ_{vis} is the visible optical depth, and we assume that the mean extinction efficiency of ice particles at a visible wavelength is 2. In Eq. (8), $< Q_e >$ is the mean extinction efficiencyiy defined by Eq. (4) for a given infrared wavelength. As the TOA outgoing radiance depends on the cloud effective particle size, four effective diameters (D_e = 10, 20, 40 and 60 μm) are specified for the radiative transfer computations. Additionally, five values of the visible optical depth (τ_{vis} = 0.03, 0.1, 0.15, 0.2, and 0.3) are specified for each particle size. A library is developed for the outgoing radiances associated with the values of the visible optical depth τ_{vis} ranging from 0.03 to 0.3 and each effective particle size.

3. Results

Figure 2 shows the observed and calculated LW and WIN band radiances and also the corresponding relative differences for each FOV. Both the observed and calculated radiances are for clear-sky conditions and their relative differences (ε) are defined as follows:

$$\varepsilon = \frac{(r_{obs} - r_{cal})}{r_{cal}} \times 100(\%) \tag{9}$$

where r is the outgoing either LW or WIN-channel radiance. The subscripts *obs* and *cal* indicate the observed and calculated quantities, respectively. The radiances computed for cloud-free FOVs are larger than their observed counterparts for both the CERES LW and WIN channels. We suggest that these differences be explained in large part by the presence of thin cirrus. An important point to note is that the cloud mask is flagged as cloudy when the assumed optical thickness of the cloud is larger than approximately 0.2 ~ 0.3 and we use only CERES FOVs declared as cloud free in the SSF product; that is, thin cirrus clouds with optical thickness less than 0.3 might be missed in the cloud detection.

The relative differences defined in Eq. (9) in the case for the LW radiance are between -2.1% and -8.3% with a mean value of -4.2%. The CERES FOVs are separated by scene type into two categories: over ocean and over land [*Loeb et al.*, 2003b]. Large differences between the measurements and simulations occur for 7 nighttime FOVs whose scene types are over land. The relative differences are approximately -8.0% for the 4 FOVs (2004070603 UTC, 36~39th FOV), and -7.0% for the other 3 FOVs (2004072903 UTC, 74~76th FOV). The relative differences in WIN channel radiances are between -1.7 and -10.6% with a mean value of -4.5%. The WIN channel radiances are calculated in the spectral range between 8.1 and 11.8 μm [*Loeb et al.*, 2003b].

Figure 3 shows both the observed and calculated LW and WIN channel radiances and their relative differences as functions of the viewing zenith angle. Both the measured and calculated radiances show the expected limb-darkening features. The angular distributions of the relative differences are similar for the LW and WIN channels. The maxima of the relative differences between the theoretical simulations and the corresponding CERES measurements seem to occur at the viewing zenith angles ranging from 25° to 30°. Evidently, the observed radiances for the pixels flagged as cloud free are smaller than the simulated data, and the relative differences can be as large as -8.3% and -10.6% for the LW and WIN band radiances, respectively, at a viewing zenith angle of ~28°. The outliers in the range between 25° and 30° may not imply something systematic but need to be further investigated with a larger set of data. These pixels are all over land. *Wilber et al.* [1999] adopted scene types from the International Geosphere Biosphere Programme (IGBP) and developed surface emissivity maps to account for the scene

dependence. Surface condition parameters in the CERES SSF products are obtained from their surface maps. Since a CERES FOV has a 20km spatial resolution at nadir, the heterogeneity of the surface emissivity over a CERES FOV could cause some errors in determining the surface parameters.

Figure 4 shows both the observed and calculated LW and WIN channel anisotropy factors and also their relative differences as functions of the viewing zenith angle. The anisotropy factors for the LW and WIN radiation are calculated from:

$$A(\theta) = \frac{\pi I(\theta)}{F}, \tag{10}$$

where θ is the viewing zenith angle, $I(\theta)$ and F are radiance and the corresponding flux at a reference level, respectively. The ADMs are used to obtain the LW and WIN broadband fluxes from the observed radiances. There are 45 ADMs for clear-sky daytime and nighttime conditions over various surfaces. As shown in Fig. 4 (the upper left panel for the LW channel and the lower panel for the WIN channel), the anisotropic factor decreases as the viewing zenith angle increases.

For the viewing zenith angles between 0° and 50°, the values of the anisotropic factors for the observed radiances are larger than those calculated except for some pixels for the viewing zenith angles larger than 27° for the LW bands. The relative differences between the measurements and simulations become smaller for both the LW and WIN bands as the viewing zenith angle approaches to 50°. The relative differences of the anisotropy factor for the LW band are between -0.23% (at θ = 45.5°) and 0.76% (at θ = 0.1°) with a mean value of 0.19%, and for the WIN band between 0.29% (at θ = 45.5°) and 2.5% (at θ = 0.1°) with a mean value of 1.26%. The TOA flux for a clear sky might be underestimated with a larger anisotropy factor. As an example using a typical clear-sky LW flux of 300 Wm^{-2}, if the CERES anisotropic factor is overestimated by a typical value of 0.2% because of potential cirrus contamination, the LW flux would be underestimated by approximately 0.2%, or 0.6 Wm^{-2}, in the regions where these cirrus clouds are present. *Loeb et al.* [2003a] showed that the difference between direct integration and the flux converted from the radiance using the LW ADMs is below 0.5

Wm^{-2}. The values of the LW anisotropy factor in the present study show quite small relative differences, which means that the differences of the anisotropy factor values between the CERES SSF products and the simulated could be within the uncertainty range of the ADM models.

Figure 5 (a) shows the inferred optical depth from minimizing the differences between the observed and calculated LW radiance as a function of the viewing zenith angle. The inferred optical thickness for each FOV is essentially below 0.3 for each D_e value. For more than 70 of the FOVs, the optical thicknesses are below 0.2, which also depend on D_e. For the viewing zenith angles between 25° and 30°, the optical thicknesses are larger than those at other angles. This is not unexpected, given the results of Fig. 3 (i.e. the difference between the observed and calculated radiance is large). Fig. 5 (b) shows the inferred cirrus optical thickness obtained by minimizing the differences between the observed and the calculated WIN channel radiances as a function of the viewing zenith angle. The optical thickness pertaining to each FOV tends to be below 0.3 with an exception of just two FOVs (τ_{vis} = 0.31 and 0.34) when D_e = 10 μm. As the effective diameter increases, the values of the optical thickness converge for both the LW and WIN channels. This feature is associated with the variation of the averaged single-scattering properties of droxtals shown in Fig. 1.

In Fig. 6, the left panels show the histograms of cirrus optical thicknesses inferred from the differences between the observed and calculated LW radiances. As the effective diameter increases, the distribution of the optical thickness is shifted towards smaller values (see Table 1) and the distribution narrows. The optical thickness distribution is similar to that of *Dessler and Yang* [2003; see their Fig. 3] for the frequent occurrence of thin cirrus clouds. The right panels in Fig. 6 show the distributions of optical thicknesses inferred from the differences between the observed and calculated WIN channel radiances. Similar to the cases pertaining to the left panels in Fig. 6, the distribution of the optical thickness derived from the WIN band also shifts to smaller values with an increase of the effective diameter (see Table 1). The peaks of the frequency distributions of the optical thickness are shifted to slightly smaller values.

Figure 7 shows clear-strong and clear-weak percent coverage of each CERES FOV. In the CERES cloud mask, there are several clear subcategories such as clear-strong and

clear-weak. The CERES SSF products provide cloud mask information on clear-strong (or, weak) percent coverage. Note that, for the CERES data, the clear-strong (or, weak) percent coverage is a weighted percentage of clear-strong (or, weak) MODIS pixels within the CERES FOV. For the data set used in this study, 70 FOVs out of the 76 FOVs have over 90% clear-strong coverage and 66 FOVs have 100% clear-strong coverage. The ratio of clear-weak percent coverage to clear-strong percent coverage is almost zero except for a few FOVs.

4. Sensitivity Study

The radiative transfer simulations require knowledge of the surface temperature and emissivity, and the vertical atmospheric temperature and water vapor profiles. We performed various sensitivity studies for clear-sky conditions with a ±1 K bias of the surface temperature, a ±2% bias of the surface emissivity, a ±1 K bias of the vertical sounding temperature, and a ±5% bias of water vapor in the lower atmospheric layers in conjunction with a ±50% bias of water vapor in the upper atmospheric layers.

Figures 8-11 show both the observed and calculated radiances as well as their relative differences for both the LW and WIN bands. The radiances are calculated with a ±2% bias of the surface emissivity (Fig. 8). Although a ±2% bias of the surface emissivity is considered, the calculated LW and WIN channel radiances are larger than their observed counterparts. The average relative differences of the observed and calculated LW (WIN) channel radiance are -3.57% (-3.11%) with a -2% bias of the surface emissivity and -4.6% (-5.5%) with a +2% bias of the surface emissivity. The CERES instrument accuracy requirements are 0.6 $Wm^{-2}Sr^{-1}$ for the LW band and 0.3 $Wm^{-2}Sr^{-1}$ for the WIN band [*Lee et al.*, 1997], which are indicated as the error bars in Figs. 8-11.

In Fig. 9 the LW and WIN channel radiances are calculated with a ±1 K bias of the surface temperature. The average relative difference of the observed and calculated LW (WIN) channel radiances are –3.62% (-3.22%) with a –1K bias of the surface temperature and -4.74% (-5.68%) with a +1K bias of the surface temperature. The effects of a +1 K (-

1 K) bias in the surface temperature and a +2% (-2%) bias in the surface emissivity are similar for both the LW and WIN channel radiances.

The LW and WIN channel radiances are calculated assuming a ±1 K bias in a given vertical temperature profile (Fig. 10). The average relative difference in the LW (WIN) channel radiances between the observed and calculated values is –3.47% (-4.29%) with a –1K bias of the temperatures and –4.9% (-4.76%) with a +1 K bias of temperatures. A +1K (-1K) bias of the vertical temperature profile causes the changes in the LW channel radiances with a similar order to the case for a +2% (-2%) bias of the surface emissivity, and little influence on the WIN channel radiances.

The LW and WIN channel radiances are calculated with a ±5% bias in the water vapor amount for lower tropospheric layers in conjunction with a ±50% bias in the water vapor amount for upper tropospheric layers (Fig 11). An upper (lower) tropospheric layer in this study is defined as one in which the temperature is below (above) 273 K. The average relative difference of the LW (WIN) channel radiances between the observed and calculated values is –6.12% (-4.83%) with a negative bias of water vapor and –2.87% (-4.25%) with a positive bias of water vapor. Both the negative (positive) bias of water vapor and a +1K (-1K) bias in the vertical temperature profile cause some changes on the LW channel radiance but have little effects on the WIN channel radiance. Since the radiance in the window region is less sensitive to water vapor amount, the variability of the radiance in the LW channel is larger than that in the WIN channel.

5. Discussion and conclusions

We investigate a set of 76 CERES FOVs that are deemed to be free of clouds by the operational CERES cloud clearing procedure. The clear-sky radiances are calculated using a forward radiative transfer model and compared to the measured radiances. The temperature and humidity profiles are taken from the rawinsondes launched during the CRYSTAL-FACE campaign in July 2002. We find that the calculated LW and WIN channel radiances are larger than those measured by CERES. A possible mechanism for these differences could be the presence of thin cirrus clouds. Clouds with optical

thicknesses less than approximately 0.2 to 0.3 are difficult to detect and much less analyze.

In the present analyses of CERES data, the cirrus optical thicknesses range generally between $0.03 < \tau_{vis} < 0.3$. It seems that thin cirrus clouds were ubiquitous in this region around Florida during CRYSTAL-FACE. The results obtained herein are somewhat similar to the result by *Dessler and Yang* [2003] who noticed that about one third of the MODIS pixels flagged as confidently clear actually contained detectible thin cirrus. As their study used the MODIS 1.38 μm band, their approach is not applicable for analyzing nighttime data. The present study is focused on a set of 76 CERES FOVs rather than the large number of daytime MODIS pixels ($>10^7$) and wide geographical region (tropical area) encompassed in their study. We find that as ice cloud effective diameter increases, the optical thickness inferred from both the LW and WIN channels converges. This study is complementary to *Dessler and Yang* [2003], as they used daytime MODIS observations and most of the CERES FOVs used in this study are for nighttime.

The anisotropic factors show some differences between the observed and calculated values at the LW and WIN bands. The comparison shows that the difference decreases with increasing the viewing zenith angle to 50°. Since anisotropy factors of the observed radiances are larger than those of the calculated radiances for the viewing zenith angles between 0° and 50°, it is likely possible to underestimate (by a few percent) CERES LW and WIN fluxes that are associated with the scenes that flagged as cloud free. The difference in the anisotropic factors is small compared to the corresponding large difference in radiance between the CERES observations and the theoretical calculations. The error in flux is related to the error in anisotropic factor. If the CERES anisotropic factor is overestimated by a typical value of 0.2% due to the neglect of the presence of thin cirrus clouds within the CERES FOVs, the LW flux would be underestimated by approximately 0.2%, or 0.6 Wm^{-2}, given a typical clear-sky LW flux of 300 W/m^2. An error would arise in the interpretation of the flux since the FOV is classified as clear sky rather than cloudy.

A sensitivity study showed that even by accounting for the uncertainties caused by several factors (excluding the presence of cirrus), such as in the temperature and humidity profiles, there is still some disagreement between the simulated for both the LW and

WIN channel radiances under clear-sky conditions and their CERES observed counterparts.

While *Dessler and Yang* [2003] showed thin cirrus clouds are ubiquitous using a daytime data set, thin cirrus clouds could also be common over Florida region at nighttime. Therefore, the radiances measured for the FOVs that are identified as "clear-sky" could be contaminated by the existence of thin cirrus clouds with optical thickness less than 0.3. Further research using active measurements during nighttime conditions would be quite useful.

Acknowledgements

The authors thank Andrew Dessler for useful comments and suggestions. This research is supported by the National Science Foundation (NSF) CAREER Award research grant (ATM-0239605), a research grant from the NASA Radiation Sciences Proram (NNG04GL24G), and a subcontract from Science Applications International Corporation (4400053274).

References

Ackerman, S. A., K. I. Strabala, W. P. Menzel, R. A. Frey, C. C. Moeller, and L. E. Gumley (1998), Discriminating clear sky from clouds with MODIS, *J. Geophys. Res., 103*, 32141-32157.

Baum, B. A., A. J. Heymsfield, P. Yang, and S. T. Bedka (2005), Bulk scattering models for the remote sensing of ice clouds. 1: Microphysical data and models. J. Appl. Meteorol. (in press).

Chepfer, H., G. Brogniez, and Y. Fouquart (1998), Cirrus clouds microphysical properties deduced from POLDER observations, *J. Quant. Spectrosc. Radiat. Transfer, 60*, 375-390.

Chepfer, H., P. Goloub, J. Riedi, J. F. De Hann, J. W. Hovenier, and P. H. Flamant (2001), Ice crystal shapes in cirrus clouds derived from POLDER/ADEOS-1, *J. Geophys. Res., 106,* 7955-7966.

Dessler, A. E., P. Yang (2003), The Distribution of tropical thin cirrus clouds inferred from Terra MODIS data, *J. Clim., 16*, 1241-1247.

Foot, J. S. (1988), Some observations of the optical properties of clouds: II. Cirrus, *Quart. J. Roy. Meteor. Soc. 114*, 145-164.

Francis, P. N., A. Jones, R. W. Saunders, K. P. Shine, A. Slingo, Z. Sun (1994), An observational and theoretical study of the radiative properties of cirrus: Some results from ICE'89, *Quart. J. Roy. Meteor. Soc. 120,* 809-848.

Fu, Q. (1996), An accurate parameterization of the solar radiative properties of cirrus clouds for climate models, *J. Clim., 9*, 2058-2082.

Fu, Q., W. B. Sun and P. Yang (1999), On model of scattering and absorption by cirrus nonspherical ice particles at thermal infrared wavelength, *J. Atmos. Res., 56*, 2937-2947.

Gao, B.-C., P. Yang, W. Han, R.-R. Li, and W. Wiscombe (2002), An algorithm using visible and 1.38 channels to retrieve cirrus reflectances from aircraft and satellite data, *IEEE Trans. Geosci. Remote Sensing, 40,* 1659-1668.

Geier, E. B., R. N. Green, D. P. Kratz, P. Minnis, W. F. Miller, S. K. Nolan, C. B. Franklin (2003), Clouds and the Earth's Radiant Energy System (CERES) Data

Management System: Single Satellite Footprint TOA/Surface Fluxes and Clouds (SSF) Collection Document, http://asd-www.larc.nasa.gov/ceres/collect_guide, 243pp.

Hansen, J. E. (1971), Multiple scattering of polarized light in planetary atmospheres. Part II. Sunlight reflected by terrestrial water clouds, *J. Atmos. Sci., 28,* 1400-1426.

Hansen, J. E., and L. D. Travis (1974), Light scattering in planetary atmosphere, *Space Sci. Rev.*, *16*, 527-610.

Heidinger, A. (1998), Nadir sounding of clouds and aerosol in the O2 A-band, Atmos. Sci. Pap. 650, 226 pp., Colo. State Univ., Fort Colins, Colo.

Jensen, E., D. Starr, and O. B. Toon (2004), Mission investigates tropical cirrus clouds, *Eos Trans. AGU, 85(5)*, 45, 50.

Kahn, B. H., K. N. Liou, S. Y. Lee, E. F. Fishbein, S. Desouza-Machado, A. Eldering, E. J. Fetzer, S. E. Hannon, L. L. Strow (2005), Nighttime cirrus detection using atmospheric infrared sounder window channels and total column water vapor, *J. Geophys. Res., 110(D7),* 07203, doi: 10.1029/2004JD005430.

King, M. D., W. P. Menzel, Y. J. Kaufman, D. Tanré, B. C. Gao, S. Platnick, S. A. Ackerman, L. A. Remer, R. Pincus, and P. A. Hubanks (2003), Cloud and Aerosol Properties, Precipitable Water, and Profiles of Temperature and Humidity from MODIS, *IEEE Trans. Geosci. Remote Sensing, 41,* 442-458.

Lee III, R. B., B. R. Barkstrom, G. L. Smith, J. E. Cooper, L. P. Kopia, and R. W. Lawrence (1996), The Clouds and the Earth's Radiant Energy System (CERES) sensors and preflight calibration plans, *J. Atmos. Oceanic Tech., 13*, 300-313.

Lee, R. B., B. R. Barkstrom, D. A. Crommclynck,G. L. Smith, W. C. Bolden, J. Paden, D. K. Pandey, S. Thomas, L. Thornhill, R. S. Wilson, K. A. Bush, P. C. Hess, and W. L. Weaver (1997), Clouds and the Earth's Radiant Energy System (CERES) Algorithm Theoretical Basis Document: Instrument Geolocate and Calibrate Earch Radiances (Subsystem 1.0), http://asd-www.larc.nasa.gov/ATBD/ATBD.html, 84 pp.

Loeb, N. G., S. Kato, K. Loukachine, and N. M. Smith (2005), Angular distribution models for top-of-atmosphere radiative flux estimation from the Clouds and the Earth's Radiant Energy System instrument on the *Terra* Satellite, 1, Methodology, *J. Atmos. Oceanic Tech., 22*, 338-351.

Loeb N. G., K. Loukachine, N. Manalo-Smith, B. A. Wielicki, and D. F. Young (2003a), Angular Distribution Models for Top-of-Atmosphere Radiative Flux Estimation from the Clouds and the Earth's Radiant Energy System Instrument on the Tropical Rainfall Measuring Mission Satellite. Part II: Validation. *J. Appl. Meteor.*, 42, 1748-1769.

Loeb, N. G., K. J. Priestley, D. P. kratz, E. B. Geier, R. N. Green, B. A. Wielicki, P. O. Hinton, and S. K. Nolan (2001), Determination of unfiltered radiances from the clouds and the earth's radiant energy system instrument, *J. Appl. Meteorol., 40*, 822-835.

Loeb, N. G., N. M. Smith, S. Kato, W. F. Millfer, S. K. Gupta, P. Minnis, and B. A. Wielicki (2003b), Angular distribution models for top-of-atmosphere radiative flux estimation from the Clouds and the Earth's Radiant Energy System Instrument on the Tropical Rainfall Measuing Mission Satellite, 1, Methodology, *J. Appl. Meteorol., 42*, 240-265.

Mather, J. H., T. P. Ackerman, M. P. Jensen, and W. E. Clements (1998), Characteristics of the atmospheric state and the surface radiation budget at the tropical western Pacific ARM site. *Geophys. Res. Lett., 25*, 4513-4516.

McFarquhar, G. M., A. J. Heymsfield, J. Spinhirne, and B. Hart (2000), Thin and subvisual tropopause tropical cirrus: observations and radiative impacts, *J. Atmos. Sci., 57*, 1841-1853.

Meyer, K., P. Yang, and B.-C. Gao (2004), Optical thickness of tropical cirrus clouds derived from the MODIS 0.66- and 1.375 channels, *IEEE. Trans. Geosci. Remote Sensing*, *42*, 833-841.

Minnis, P., D. F. Young, D. P. Kratz, J. A. Coakley, Jr., M. D. King, D. P. Garber, P. W. Heck, S. Mayor, and R. F. Arduini (1997), Clouds and the Earth's Radiant Energy System (CERES) Algorithm Theoretical Basis Document: Cloud Optical Property Retrieval (Subsystem 4.3), http://asd-www.larc.nasa.gov/ATBD/ATBD.html, 60 pp.

Minnis, P., D. F. Young, S. Sun-Mack, P. W. Heck, D. R. Doelling, and Q. Trepte (2003), CERES Cloud Property Retrievals from Imagers on *TRMM*, *Terra*, and Aqua, Proc. SPIE 10th International Symposium on Remote Sensing: Conference on

Remote Sensing of Clouds and the Atmosphere VII, Barcelona, Spain, 8-12 September, 37-48.

Mitchell, D. L. (2002), Effective diameter in radiation transfer: General definition, applications, and limitations, *J. atmos. Sci, 59*, 2330-2346.

Platnick, S., M. D. King, S. A. Ackerman, W. P. Menzel, B. A. Baum, J. C. Riédi, and R. A. Frey (2003), The MODIS Cloud Products: Algorithms and Examples from Terra, *IEEE Trans. Geosci. Remote Sensing*, *41*, 459-473.

Prabhakara, C., D. P. Kratz, J. M. Yoo, G. Dalu, and A. Vernekar (1993), Optically thin cirrus clouds: radiative impact on the warm pool, *J. Quant. Spectrosc. Radiat. Transfer*, *49*, 467-483.

Roskovensky, J. K., and K. N. Liou (2003), Detection of thin cirrus from 1.38 μm / 0.65 μm reflectance ratio combined with 8.6-11 μm brightness temperature difference, *Geophys. Res. Lett., 30(19)*, 1985, doi:10.1029/2003GL018135.

Rossow, W. B. and R. A. Schiffer (1991), ISCCP cloud data products, *Bull. Am. Meteorol. Soc.*, *72*, 2-20.

Rothman, L. S., C. P. Rinsland, A. Goldman, S. T. Massie, D. P. Edwards, J. -M. Flaud, A. Perrin, C. Camy-Peyret, V. Dana, J. -Y. Mandin, J. Schroeder, A. McCann, R. R. Gamache, R. B. Wattson, K. Yoshino, K. V. Chance, K. W. Jucks, L. R. Brown, V. Nemtchinov, and P. Varanasi (1998), The HITRAN Molecular Spectroscopic Database and HAWKS (HITRAN Atmospheric Workstation): 1997 edition, *J. Quant. Spectrosc. Radiat. Transfer, 60*, 665-710.

Sassen, K., M. K. Griffin, and G. C. Dodd (1989), Optical scattering and microphysical properties of subvisual cirrus clouds and climatic implications, *J. Appl. Meteorol., 28*, 91-98.Smith, G. L., N. Manalo-Smith, L. M. Avis (1994), Limb-darkening models from along-track operation of the ERBE scanning radiometer, *J. Appl. Meteorol., 33*, 74-84.

Smith, G. L., B. A. Wielicki, B. R. Barkstrom, R. B. Lee, K. J. Priestly, T. P. Charlock, P. Minnis, D. P. Kratz, N. Loeb, and D. F. Young (2004), Clouds and earth radiant system: an overview, *Adv. Space Res., 33*, 1125-1131.

Stamnes, K., S. C. Tsay, W. Wiscombe, and K. Jayaweera (1988), A numerically stable algorithm for discrete-ordinate-method radiative transfer in multiple scattering and emitting layered media, *Appl. Opt., 27*, 2502-2509.

Tobin, D. C., F. A. Best, P. D. Brown, S. A. Clough, R. G. Dedecker, R. G. Ellingson, R. K. Garcia, H. B. Howell, R. O. Knuteson, E. J. Mlawer, H. E. Revercomb, J. F. Short, P. F. W. van Delst, and V. P. Walden (1999), Downwelling spectral radiance observations at the SHEBA ice station: water vapor continuum measurements from 17 to 26 μm, *J. Geophys. Res., 104*, 2081-2092.

Trepte, Q., Y. Chen, S. Sun-Mack, P. Minnis, D. F. Young, B. A. Baum, and P. W. Heck (1999), Scene identification for the CERES cloud analysis subsystem, Proc. AMS 10th Conf. Atmos. Rad., Madison, WI, 28 June - 2 July, 169-172.

Wang, P.-H., M.P. McCormick, L. R. Poole, W. P. Chu, G. K. Yue, G. S. Kent, and K. M. Skeens (1994), Tropical high cloud characteristics derived from SAGE II extinction measurements, *Atmos. Res., 34*, 53-83.

Wang, P.-H., P. Minnis, M. P. McCormick, G.S. Kent and K. M. skeens (1996), A 6-year climatology of cloud occurrence frequency from Stratospheric Aerosol and gas Experiment II observations (1985-1990), *J. Geophys. Res., 101*, 29407-29429.

Warren, S. G. (1984), Optical constants of ice from the ultraviolet to the microwave, *Appl. Opt., 23*, 1206-1225.

Wielicki, B. A., B. R. Barkstrom, E. F. Harrison, R. B. Lee III, G. L. Smith, and J. E. Cooper (1996), Clouds and the earth's radiant energy system (CERES): An earth observing system experiment, *Bull. Am. Meteorol. Soc., 77*, 853-868.

Wilber, A. C., D. P. Kratz, and S. K. Gupta (1999), Surface emissivity maps for use in satellite retrievals of longwave radiation, NASA/TP-1999-209362, NASA, Washington, DC, 35 pp.

Winker, D. M., and C. R. Trepte (1998), Laminar cirrus observed near the tropical tropopause by LITE, *Geophys. Res. Lett., 25*, 3351-3354.

Yang, P., B. A. Baum, A. J. Heymsfield, Y. X. Hu, H.-L. Huang, S.-C. Tsay, S. Ackerman (2003a), Single-Scattering properties of droxtals, *J. Quant. Spectrosc. Radiat. Transfer, 79-80*, 1159-1169.

Yang, P., M. G. Mlynczak, H, Wei, D. P. Kratz, B. A. Baum, Y. X. Hu, W. J. Wiscombe, A. Heidinger, and M. I. Mishchenko (2003b), Spectral signature of ice clouds in the far-infrared region: Single-scattering calculations and radiative sensitivity study, *J. Geophys. Res., 108(D108)*, 4569, doi:10.1029/2002JD003291.

Yang, P., H. Wei, H.-L. Huang, B. A. Baum, Y. X. Hu, G. W. Kattawar, M. I. Mishchenko, and Q. Fu (2005), Scattering and absorption properties of various nonspherical ice particles in the infrared and far-infrared spectral region, *Appl. Opt.*, *44*, 5512-5523.

Zhang, Z. B., P. Yang, G. W. Kattawar, S.-C. Tsay, B. A. Baum, Y. X. Hu, A. J. Heymsfield, and J. Reichardt (2004), Geometric Optics Solution to light scattering by droxtal ice crystals, *Appl. Opt., 43*, 2490-2499.

Table 1. The average optical depths of thin cirrus clouds retrieved from the differences of the observed and calculated longwave and window band radiances for four effective diameters.

	$D_e = 10\,\mu m$	$D_e = 20\,\mu m$	$D_e = 40\,\mu m$	$D_e = 60\,\mu m$
Longwave	0.149	0.120	0.105	0.100
Window	0.146	0.113	0.091	0.083

Figure 1. Averaged extinction efficiency, absorption efficiency and asymmetry factor for droxtal ice crystals with sizes of 10, 20, 40, and 60 μm in the spectral region from 50 to 2000 cm^{-1}.

Figure 2. (a) The observed and calculated TOA outgoing longwave band radiances, (b) the relative differences for the computed and observed outgoing longwave band radiances, (c) the window band radiance, (d) relative differences for the computed and observed outgoing window band radiances. CERES FOVs flagged as cloud free have been chosen, which are located within 0.25 degree in both latitude and longitude over 4 atmospheric sounding locations during CRYSTAL-FACE period (July 2002).

Figure 3. Similar to Fig. 2, except that the x-axis is for the viewing zenith angle in Fig. 3.

Figure 4. Anisotropy factors provided by the CERES SSF products in comparison with the present simulations. Panel (a) is for the longwave band and panel (b) is for the window band.

Figure 5. Optical depths of thin cirrus retrieved from the difference of the observed radiances and the simulated counterparts by assuming various effective particle sizes. Panel (a): retrieval from use of the longwave band data; panel (b) retrieval from use of the window band.

Figure 6. Distributions of the optical depths of thin cirrus clouds retrieved from the differences of the observed and simulated radiances by assuming various effective particle sizes. Left panels are based on the longwave band data; right panels are based on the window band data.

Figure 7. (a) Clear-srong coverage percent and clear-weak coverage percent and (b) the ratio clear-weak coverage to clear-strong coverage.

Figure 8. (a) The observed and calculated TOA outgoing longwave band radiances, (b) the relative differences for the computed and observed outgoing longwave band radiances, (c) the window band radiance, (d) relative differences between the computed and observed outgoing window band radiances. The radiances are calculated with a bias of ±2% in the surface emissivity. The error bars 0.6 $Wm^{-2}Sr^{-1}$ for the longwave band CERES measurement and 0.3 $Wm^{-2}Sr^{-1}$ for the window band.

Figure 9. Similar to Fig. 8, except that the radiances are calculated with a bias of ±1 K in the surface temperature.

Figure 10. Similar to Fig. 8, except that the radiances are calculated with a bias of ±1 K in the vertical atmospheric temperature profile.

Figure 11. Similar to Fig. 8, except that the radiances are calculated with a bias of ±5% in lower atmospheric water vapor amount in conjunction with a ±50% in upper atmospheric water vapor amount. Biases of the same sign are considered together. (L) indicates the lower troposphere and (U) indicates the upper troposphere.

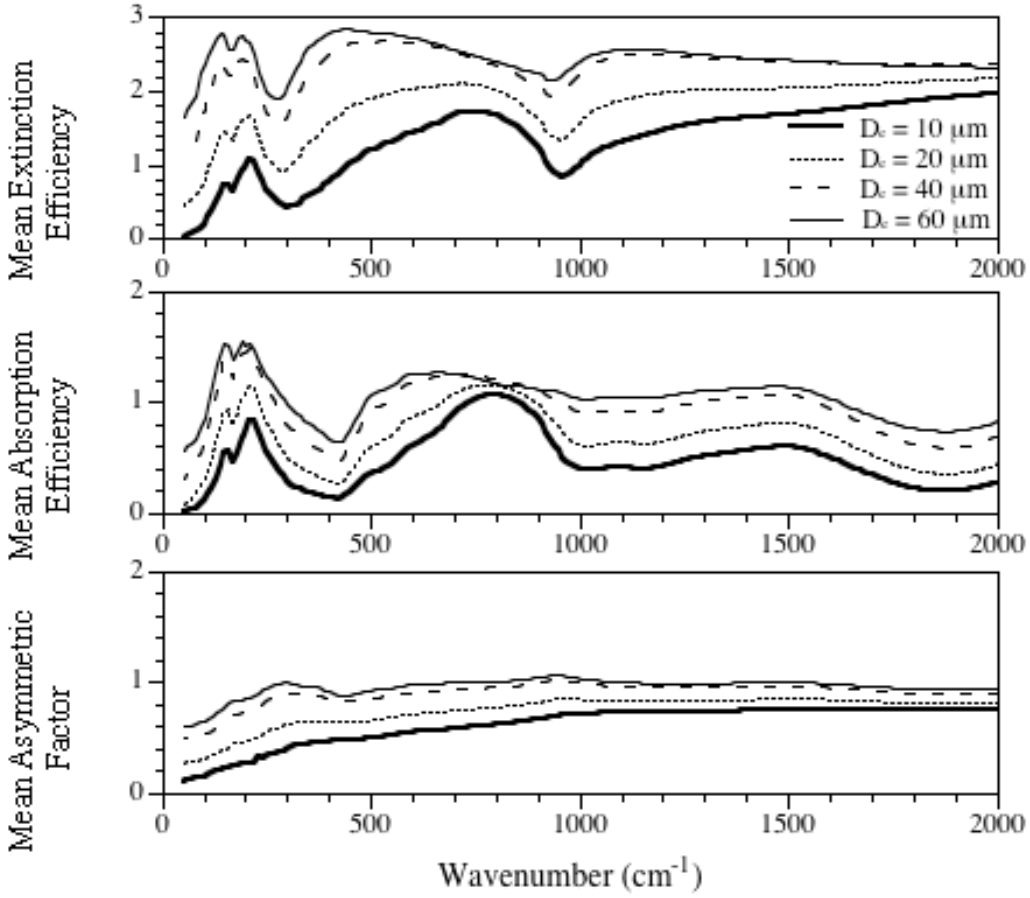
Mean Extinction Efficiency
Mean Absorption Efficiency
Mean Asymmetric Factor
Wavenumber (cm-1)
De = 10 μm
De = 20 μm
De = 40 μm
De = 60 μm
0
500
1000
1500
2000
0
1
2
3

Figure 1.

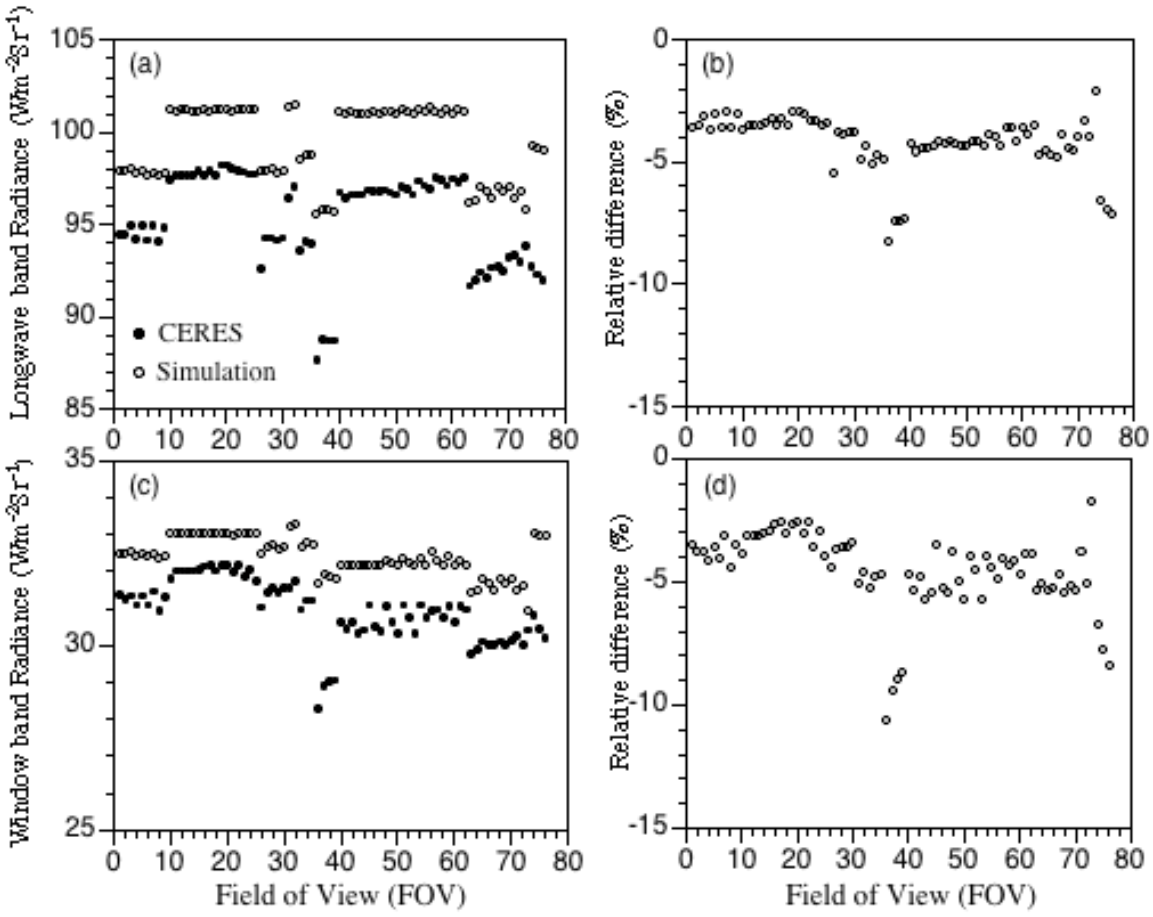
(a)
(b)
(c)
(d)
CERES
Simulation
Longwave band Radiance (Wm^{-2}Sr^{-1})
Window band Radiance (Wm^{-2}Sr^{-1})
Relative difference (%)
Field of View (FOV)
105
100
95
90
85
35
30
25
0
-5
-10
-15
0 10 20 30 40 50 60 70 80

Figure 2.

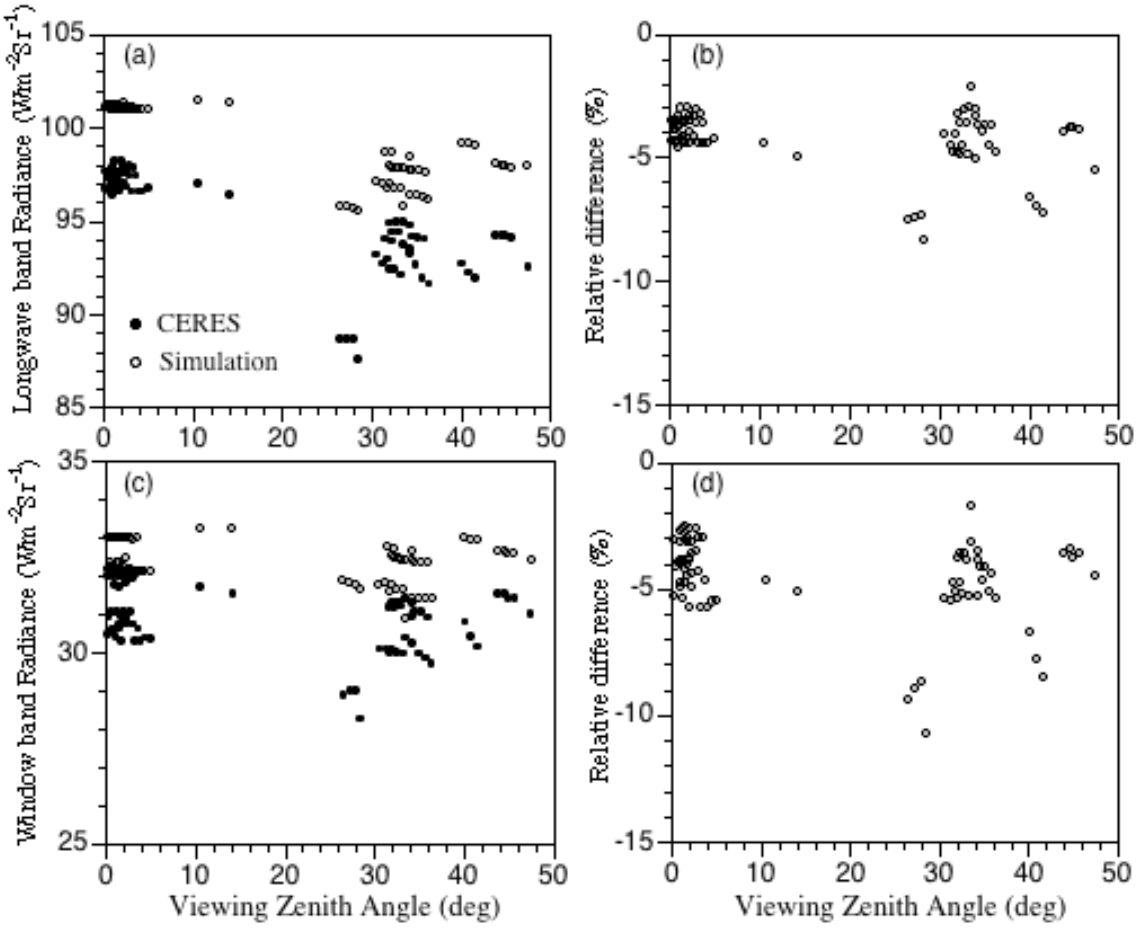
(a)
(b)
(c)
(d)
CERES
Simulation
Longwave band Radiance (Wm-2Sr-1)
Window band Radiance (Wm-2Sr-1)
Relative difference (%)
Viewing Zenith Angle (deg)
Viewing Zenith Angle (deg)

Figure 3.

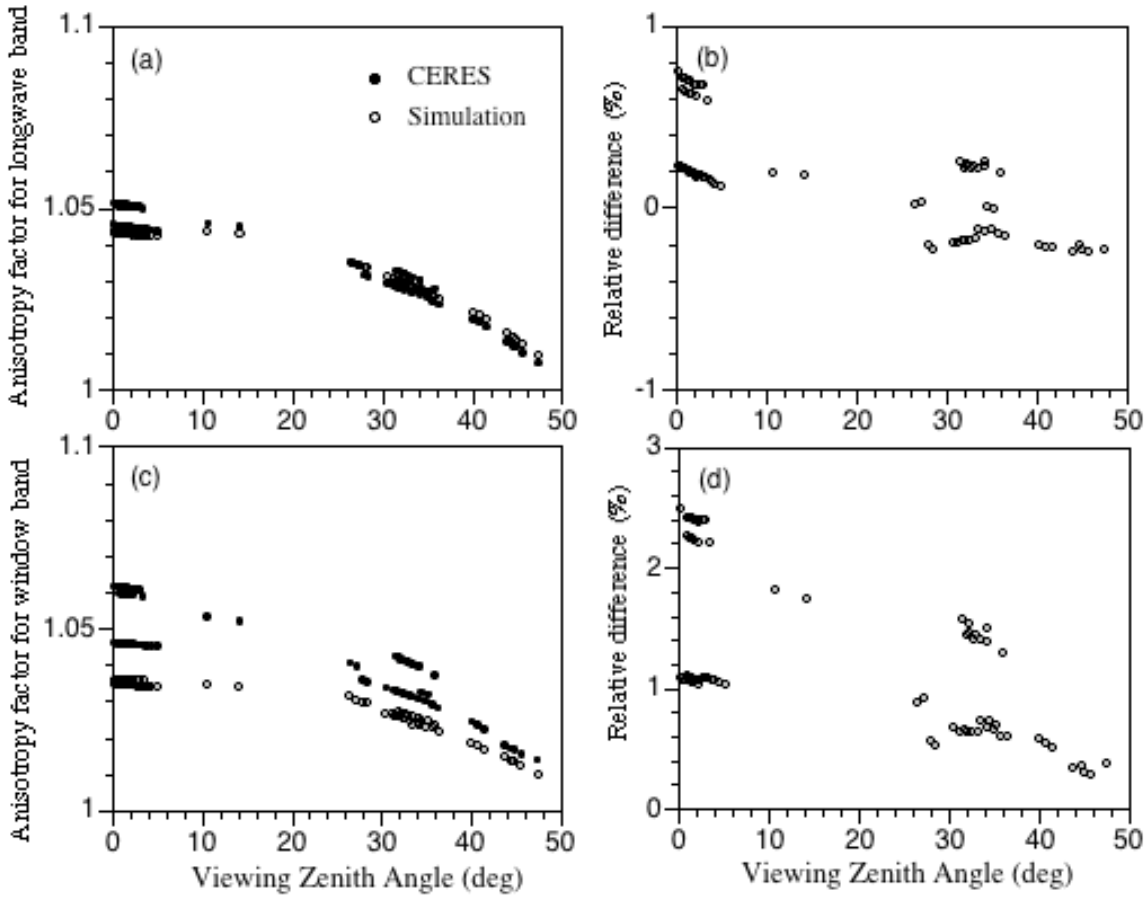
(a)
CERES
Simulation
Anisotropy factor for longwave band
(b)
Relative difference (%)
(c)
Anisotropy factor for window band
(d)
Relative difference (%)
Viewing Zenith Angle (deg)
Viewing Zenith Angle (deg)

Figure 4.

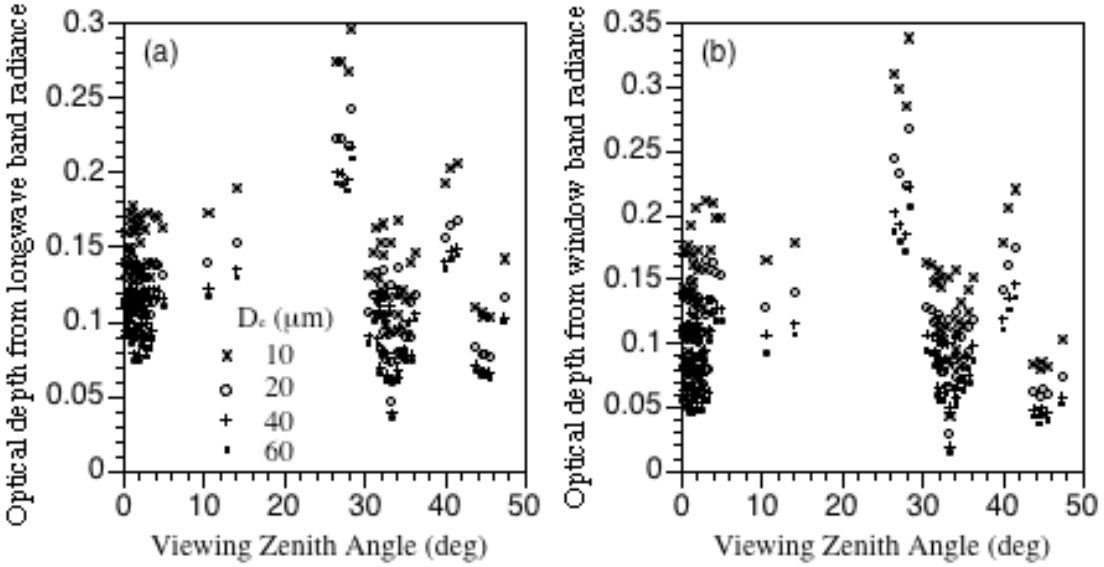
(a)
(b)
Optical depth from longwave band radiance
Optical depth from window band radiance
Viewing Zenith Angle (deg)
Viewing Zenith Angle (deg)
D_e (μm)
10
20
40
60
0
0.05
0.1
0.15
0.2
0.25
0.3
0.35
0
10
20
30
40
50

Figure 5.

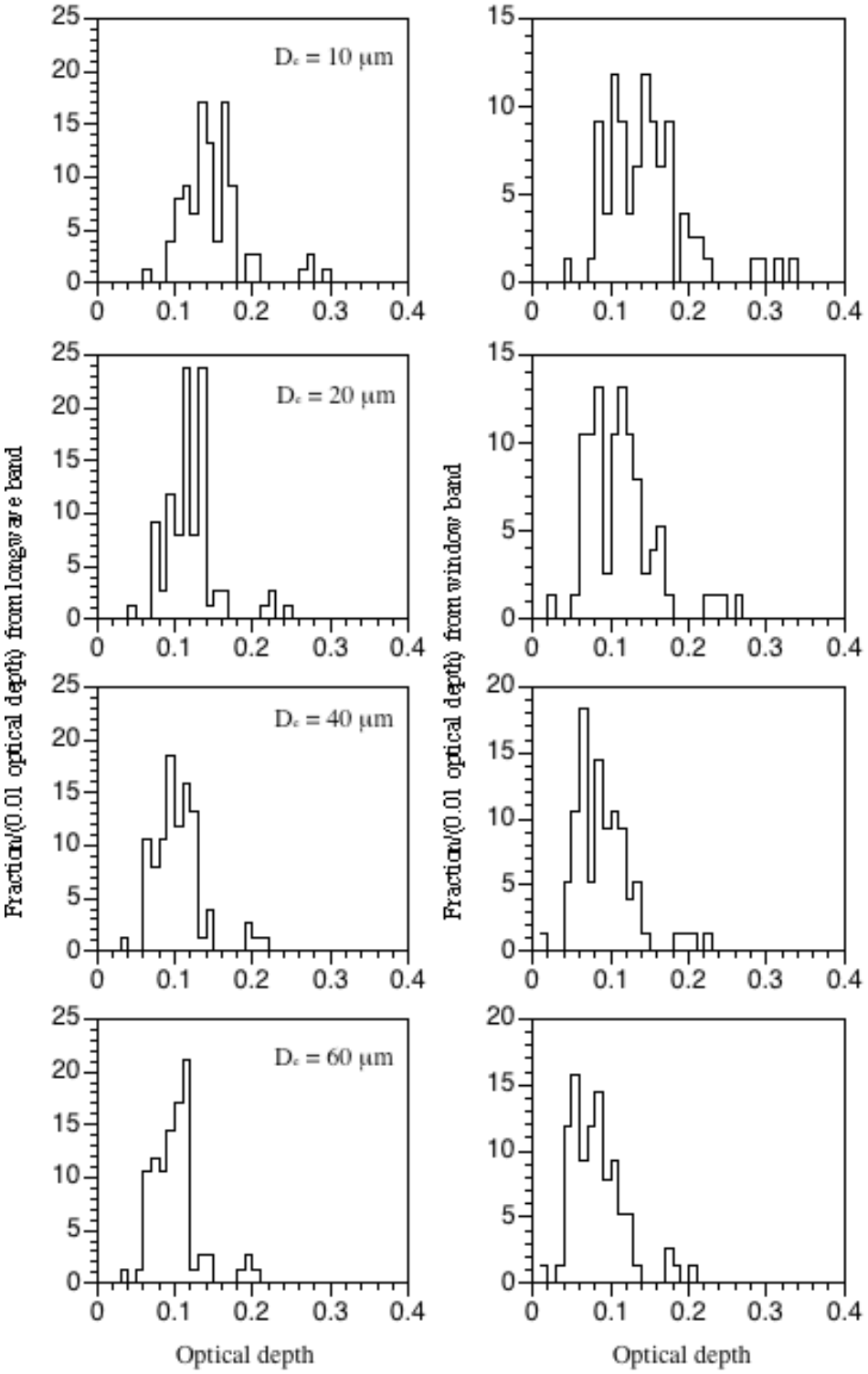
De = 10 μm
De = 20 μm
De = 40 μm
De = 60 μm
Fraction/(0.01 optical depth) from longwave band
Fraction/(0.01 optical depth) from window band
Optical depth
Optical depth

Figure 6.

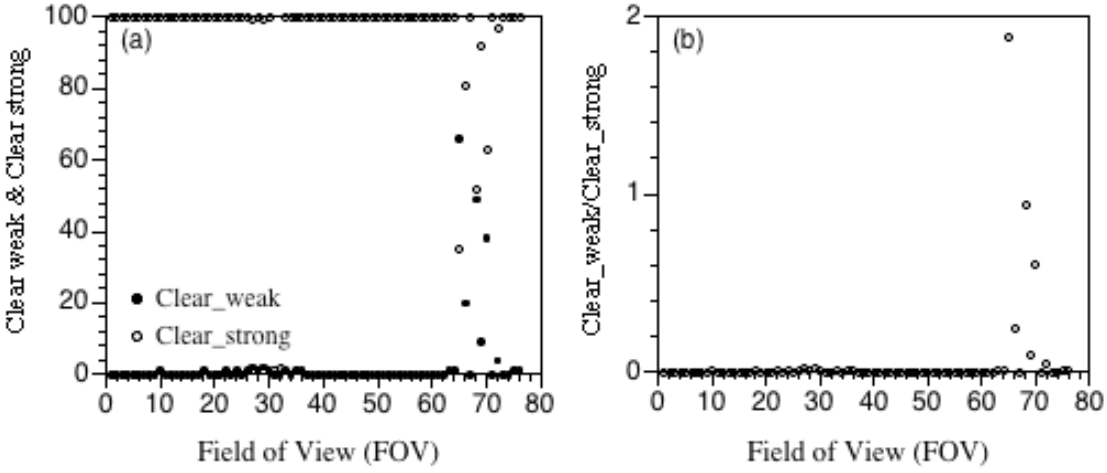
(a)
Clear weak & Clear strong
Clear_weak
Clear_strong
Field of View (FOV)
(b)
Clear_weak/Clear_strong
Field of View (FOV)

Figure 7.

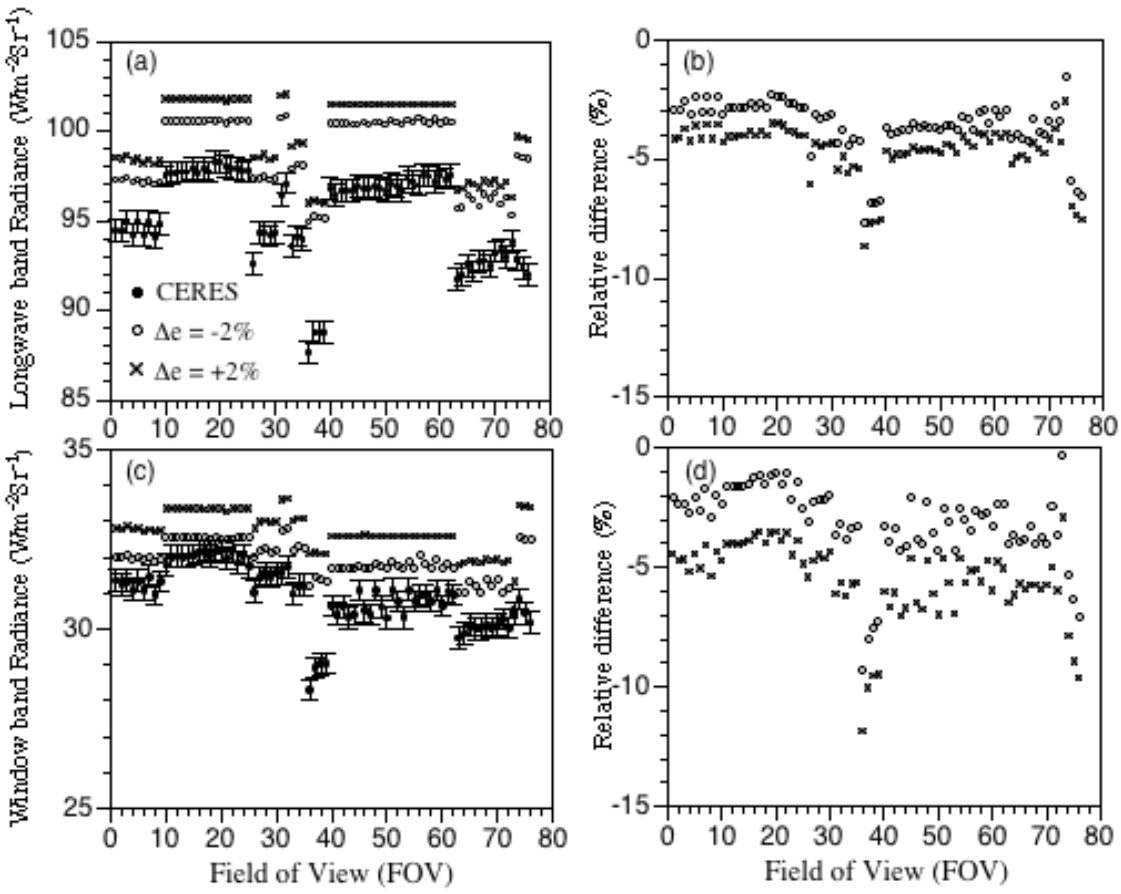
(a)
(b)
(c)
(d)
CERES
Δe = -2%
Δe = +2%
Longwave band Radiance (Wm⁻²Sr⁻¹)
Window band Radiance (Wm⁻²Sr⁻¹)
Relative difference (%)
Field of View (FOV)

Figure 8.

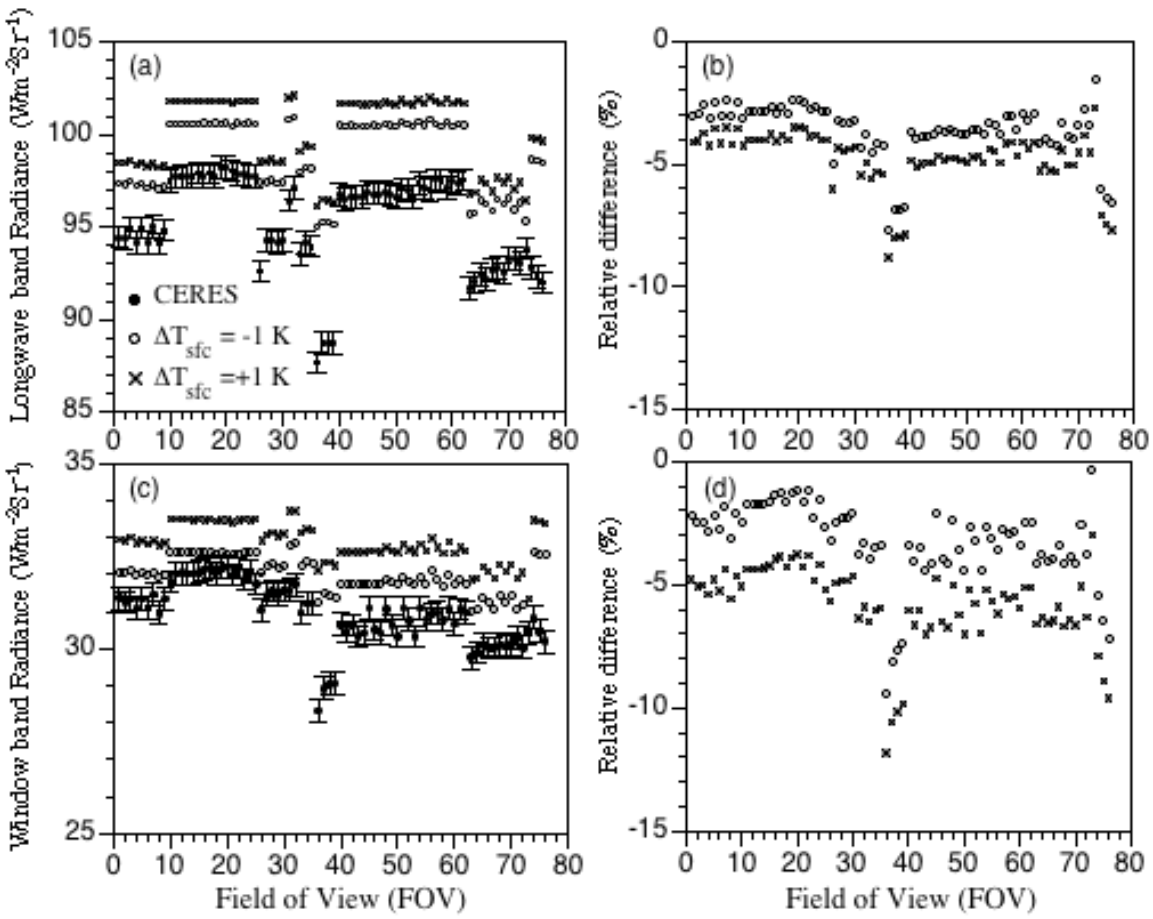
(a)
(b)
(c)
(d)
CERES
ΔT_sfc = -1 K
ΔT_sfc =+1 K
Longwave band Radiance (Wm⁻²Sr⁻¹)
Window band Radiance (Wm⁻²Sr⁻¹)
Relative difference (%)
Relative difference (%)
Field of View (FOV)
Field of View (FOV)

Figure 9.

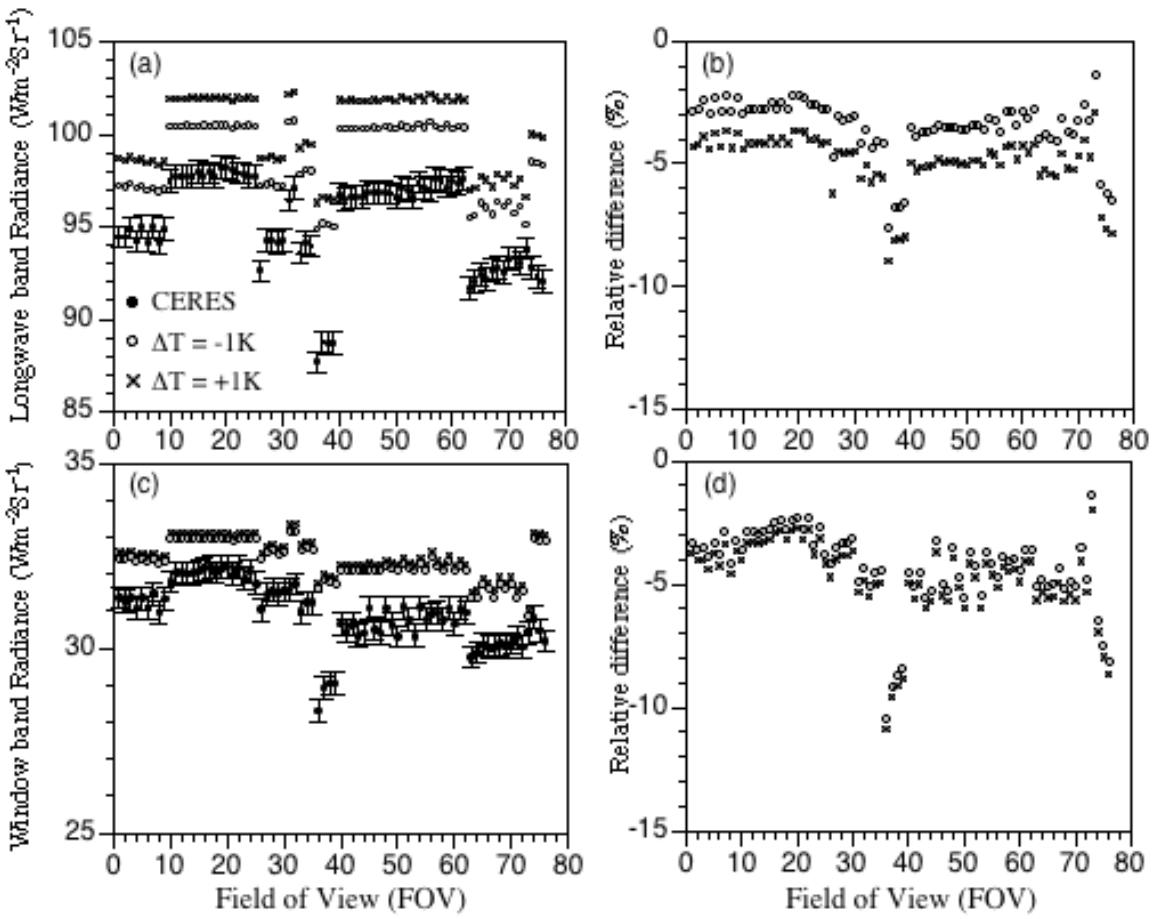
(a)
(b)
(c)
(d)
CERES
ΔT = -1K
ΔT = +1K
Longwave band Radiance (Wm⁻²Sr⁻¹)
Window band Radiance (Wm⁻²Sr⁻¹)
Relative difference (%)
Field of View (FOV)
105
100
95
90
85
35
30
25
0
-5
-10
-15
0 10 20 30 40 50 60 70 80

Figure 10.

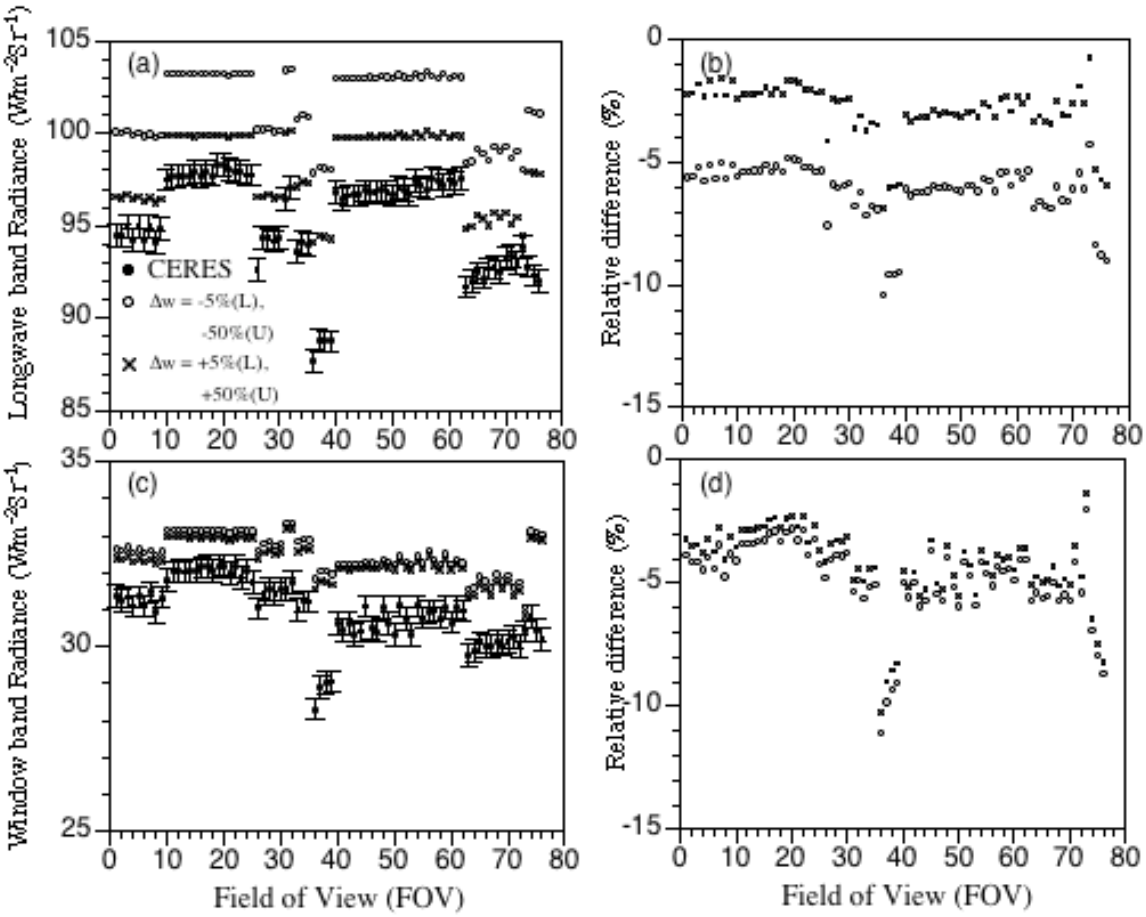
(a)
(b)
(c)
(d)
Longwave band Radiance (Wm⁻²Sr⁻¹)
Window band Radiance (Wm⁻²Sr⁻¹)
Relative difference (%)
CERES
Δw = -5%(L), -50%(U)
Δw = +5%(L), +50%(U)
Field of View (FOV)
Field of View (FOV)

Figure 11.